Evaluation of VIIRS Thermal Emissive Bands Long-Term Calibration Stability and Inter-sensor Consistency Using Radiative Transfer Modeling

Feng Zhang *, Xi Shao, Changyong Cao, Yong Chen, Wenhui Wang, Tung-Chang Liu, Xin Jing

Posted Date: 27 February 2024

doi: 10.20944/preprints202402.1582.v1

Keywords: Visible Infrared Imaging Radiometer Suite (VIIRS); NOAA-21; NOAA-20; S-NPP; radiative transfer modeling; community radiative transfer model (CRTM); thermal emissive band (TEB); calibration; observation minus background difference (O-B); double-difference method.

Article

Evaluation of VIIRS Thermal Emissive Bands Long-term Calibration Stability and Inter-Sensor Consistency Using Radiative Transfer Modeling

Feng Zhang [1], Xi Shao [1], Changyong Cao [2], Yong Chen [2], Wenhui Wang [1], Tung-Chang Liu [1], and Xin Jing [1]

[1] Cooperative Institute for Satellite Earth System Studies (CISESS, Earth System Science Interdisciplinary Center, University of Maryland, College Park, MD 20740, USA; zfsu@umd.edu(F.Z.); xshao@umd.edu (X.S.); wenhui.wang@noaa.gov (W.W); tcliu@umd.edu (T.L.); xinjing@umd.edu (X.J.)

[2] NOAA/NESDIS/Center for Satellite Applications and Research, College Park, MD 20740, USA; changyong.cao@noaa.gov (C.C.); yong.chen@noaa.gov (Y.C.)

* Correspondence: zfsu@umd.edu

Abstract: This study investigates the long-term stability of the Suomi National Polar-orbiting Partnership (S-NPP) Visible Infrared Imaging Radiometer Suite (VIIRS) moderate-resolution Thermal Emissive Bands (M TEBs; M12 – M16) covering a period from February 2012 to August 2020. It also assesses inter-sensor consistency of the VIIRS M TEBs among three satellites—S-NPP, NOAA-20, and NOAA-21 over eight months spanning from March 18 to November 30, 2023. The field of interesting is limited to the ocean surface between 60°S and 60°N, specifically under clear-sky conditions. Taking radiative transfer modeling (RTM) as the transfer reference, we employed the Community Radiative Transfer Model (CRTM) to simulate VIIRS TEB brightness temperature (BTs), incorporating European Centre for Medium-range Weather Forecasts (ECMWF) reanalysis data as inputs. Our results reveal two key findings. Firstly, the reprocessed S-NPP VIIRS TEBs exhibit a robust long-term stability, as demonstrated through analyses of the observation minus background BT differences (O-B ΔBTs) between VIIRS measurements (O) and CRTM simulations (B). The drifts of the O-B BT differences are consistently less than 0.105 K/Decade across all S-NPP VIIRS M TEB bands. Notably, observations from VIIRS M14 and M16 stand out with drifts well within 0.04 K/Decade, reinforcing their exceptional reliability for climate change studies. Secondly, excellent inter-sensor consistency among these three VIIRS instruments is confirmed through the double-difference analysis method (O-O). This method relies on the O-B BT differences obtained from daily data. The mean inter-VIIRS O-O BT differences remain within 0.08 K for all M TEBs, except for M13. Even in the case of M13, the O-O BT differences between NOAA-21 and NOAA-20/S-NPP have values of 0.312 K and 0.234 K, respectively, which are comparable to the 0.2 K difference between some TEBs among VIIRS and MODIS. These disparities are primarily attributed to the significant differences in the Spectral Response Function (SRF) of NOAA-21 compared to NOAA-20 and S-NPP. Our study confirms the RTM-based TEB quality evaluation method's versatility and effectiveness in assessing long-term sensor stability and inter-sensor consistency. The double-difference approach effectively mitigates uncertainties and biases inherent to CRTM simulations, establishing itself a robust mechanism for assessing inter-sensor consistency. In addition, we've observed that, except for M13, M12 always exhibits larger spatial variations of O-O BT differences with greater uncertainties compared to the other M TEBs. The influence of solar contribution through sea surface reflection on the Top of Atmosphere (TOA) radiance measurements during daytime in M12 should not be underestimated.

Keywords: Visible Infrared Imaging Radiometer Suite (VIIRS); NOAA-21; NOAA-20; S-NPP; radiative transfer modeling; community radiative transfer model (CRTM); thermal emissive band (TEB); calibration; observation minus background difference (O-B); double-difference method

 doi:10.20944/preprints202402.1582.v1

1. Introduction

The Visible Infrared Imaging Radiometer Suite (VIIRS) is a crucial instrument onboard the Suomi National Polar-orbiting Partnership (S-NPP) satellite, bridging NASA Earth Observing System and the next generation Joint Polar Satellite System (JPSS) platforms since its launch in November 2011 [1]. Designed for seamless continuity with the legacy of Moderate Resolution Imaging spectroradiometer (MODIS), the S-NPP VIIRS has ushered in a new era of operational environmental remote sensing, contributing significantly to scientific research and applications in Earth's land, ocean, and atmosphere studies [2–4]. More than 20 VIIRS Environmental Data Records (EDRs) have been derived from its Sensor Data Records (SDRs), providing essential data on aerosols, cloud properties, fires, albedo, snow and ice, vegetation, sea surface temperature, ocean color, and nighttime visible light applications. Rigorous verification and validation efforts have been applied to S-NPP VIIRS SDR data [5–7], and numerous studies have examined the data consistency between S-NPP VIIRS and MODIS [8–12]. These studies have demonstrated that the VIIRS Thermal Emissive Bands (TEBs) closely align with similar bands of MODIS, exhibiting differences within a 0.2 K range, emphasizing the remarkable consistency between VIIRS and MODIS observations.

Following the launch of the S-NPP satellite, two additional JPSS satellites, namely NOAA-20 and NOAA-21, were successfully launched in November 2017 and November 2022, respectively. The three VIIRSs on these satellites provide continuous Earth observations for over a decade. Detailed information on VIIRS TEB calibration algorithms, characteristics, and performance can be referenced in several prior studies [13–16]. The on-orbit VIIRS TEB calibration is performed on a scan-by-scan basis, employing a quadratic calibration algorithm. This algorithm utilizes observations from the V-grooved onboard calibrator blackbody (OBCBB) at a fixed scan-angle, with the space view (SV) providing the background offset for the calibration during each scan. Recent studies [17–19] have provided further insights into VIIRS TEB calibration.

Previous studies noted that significant differences exist in the spectral response functions (SRFs) of different instruments, such as VIIRS and MODIS. To mitigate the effects of the SRF differences, transfer references were employed, such as hyperspectral infrared sounder measurements [17], ground targets like Dome-C [10,20], or measurements from instruments like the Cross-track Infrared Sounder on SNPP and NOAA-20 spacecraft [7]. However, these intercomparison studies are limited in the number of spectral channels they can cover due to the mismatch between different instruments. In this study, following the methodology outlined by Liu et al. [21], radiative transfer modeling (RTM) has been applied as the transfer reference. The simulation of VIIRS TEB brightness temperatures (BTs) collocated with VIIRS observations is carried out using the Community Radiative Transfer Model (CRTM) [22,23]. This comprehensive evaluation covers all VIIRS M TEBs.

Two investigations with different time scales were conducted. The first study evaluates the long-term (2012-2020) stability of the NOAA STAR version 2 reprocessed S-NPP VIIRS moderate-resolution TEBs (M12-M16) data. The stability of VIIRS TEBs is crucial for the quality of downstream VIIRS environmental data record products, impacting variables like sea surface temperature and cloud products. The second study focused on analyzing the inter-sensor consistency of VIIRS TEB data among S-NPP, NOAA-20, and NOAA-21 in 2023. Notably, biases can emerge even with the same stable sensor, such as VIIRS, across different satellites. Understanding and, where possible, resolving radiometric differences of this nature are necessary [5]. Ensuring consistency among NOAA-21, NOAA-20 and S-NPP is vital for extending existing data products and creating long-term global science datasets. Hence, the stability and consistency of VIIRS TEBs, the focal points of this study, are crucial for maintaining and upholding the data quality of downstream VIIRS EDR products and advancing Earth science research and climate applications.

In the following sections, we will first introduce the methodology and the data for assessing VIIRS S-NPP TEB stability and inter-sensor VIIRS consistency in Section 2. Section 3 will present the results and analyses in detail. The conclusions and some discussions will be provided in Section 4.

2. Methodology and Data

 doi:10.20944/preprints202402.1582.v1

2.1. VIIRS Thermal Emissive Band Calibration and Characteristics

Among the 22 spectral bands of VIIRS, the five moderate-resolution TEBs (M TEBs: M12~M16, with a spatial resolution of 750 m at nadir) encompass a spectral region spanning from 3.6 to 12.5 μm. Table 1 lists the detailed VIIRS M TEB channel properties and primary applications.

Table 1. VIIRS moderate-resolution TEB channel properties and primary applications.

VIIRS TEBs	Central wavelength (μm)			Gas	Application
	NOAA-21	NOAA-20	S-NPP		
M12	3.688	3.696	3.693	H_2O	Sea surface temperature, Land surface type, Cloud mask.
M13	4.017	4.068	4.065	–	Fires,Land surface type, Cloud mask,Dust.
M14	8.571	8.580	8.577	H_2O	Sea surface temperature, Land surface type, Cloud properties, Volcanic ash.
M15	10.640	10.693	10.710	–	Sea surface temperature, Fires, VIIRS polar winds, Land surface temperature/type, Cloud properties, Cryosphere ice cover properties, Smoke/dust/volcanic ash.
M16	11.917	11.854	11.832	H_2O	Sea surface temperature, Fires, Land surface temperature/type, Cloud properties, Cryosphere ice cover properties, Volcanic ash.

The VIIRS M TEB detectors are located on a cold focal plane assembly (FPA), nominally controlled at ~80K with a passive radiative cooler. VIIRS TEBs rely on an onboard blackbody (BB) as the primary calibration source, in conjunction with the Space View (SV), which provides the instrument background reference. The calibration equation for the TEB, as detailed in the works of VIIRS SDR ATBD (https://ncc.nesdis.noaa.gov/documents/documentation/ATBD-VIIRS-RadiometricCal_20131212.pdf), converts the background-subtracted digital counts (dn) of each detector into spectral radiance entering the instrument aperture ($\overline{L_{ap}}$), which is averaged over the wavelength range covered by a spectral band. The $\overline{L_{ap}}$ is given by the following calibration equation:

$$\overline{L_{ap}} = \frac{F\sum_{i=0}^{2} c_i dn^i + (RVS_{SV} - RVS_\theta)\frac{[(1-\rho_{RTA})\overline{L_{RTA}} - \overline{L_{HAM}}]}{\rho_{RTA}}}{RVS_\theta}, \quad (1)$$

where c_i is the calibration coefficients measured prelaunch, RVS_θ the response versus scan function (RVS) at the Earth View (EV) angle of incidence on the Half Angle Mirror (HAM), ρ_{RTA} the reflectivity of the Rotating Telescope Assembly (RTA), and the $\overline{L_{RTA}}$ *and* $\overline{L_{HAM}}$ the averaged emitted radiances of the RTA and HAM, respectively. *F* represents the on-orbit degradation factor (F-factor), which varies depending on the specific detector and the side of the HAM. The calibration of EV scene radiance is adjusted to accommodate any changes in detector response by applying the *F* factor, as described in equation (1). Continuous monitoring of detector response characteristics on orbit ensures the reliability of the calibration process outlined in equation (1). For a more detailed understanding of the VIIRS TEB calibration algorithms, readers can refer to the following references: [13–15,17–19].

In this research, we employed radiative transfer modeling to assess the on-orbit stability and consistency of VIIRS M TEBs. This approach offers an independent evaluation of the onboard blackbody-based calibration accuracy, distinct from Equation (1).

Figure 1 illustrates the SRFs of the five VIIRS M TEBs, superimposed on the blackbody Planck Function curve at 292.5K, corresponding to the BB temperature during VIIRS' normal operations. Notably, the spectral response of NOAA-21 M13 differs significantly from that of NOAA-20 and S-NPP VIIRS, as depicted in Figure.1b.

 doi:10.20944/preprints202402.1582.v1

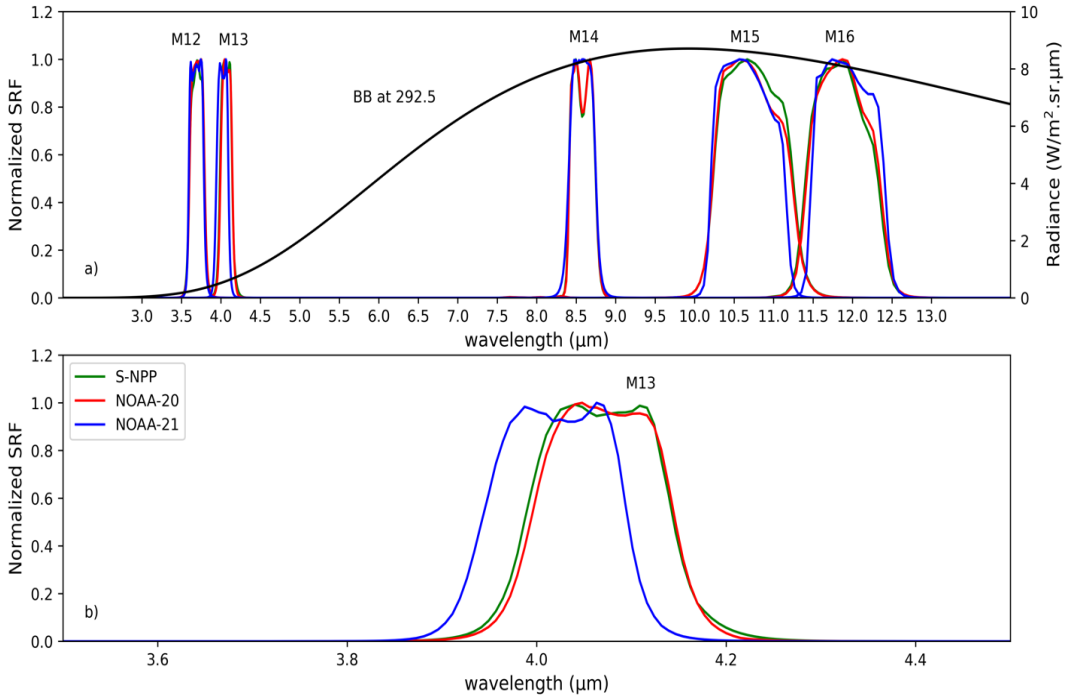

Figure 1. (a) VIIRS SRFs overlaid with blackbody Planck function curve at 292.5K; (b) Zoomed VIIRS SRFs only for band 13 (M13).

Figure 2 illustrates the weighting function profiles (a) covering all five VIIRS TEBs and (b) specifically focusing on the M13 band. The weighting function is the derivative of transmittance (τ) with respect to altitude (z), denoted as $d\tau/dz$. Here, it is derived from the 1976 US standard atmosphere model. The weighting function serves as an indicator of the predominant layer (at the surface or in the atmosphere) from which most of the radiation for a specific spectral band originates. All five M-bands (M12 to M16) clearly display their peak weighting function position at the surface level, indicating that they are primarily sensitive to surface conditions. Furthermore, except for the M13, all other bands exhibit minor differences in their weighting function profiles among S-NPP, NOAA-20, and NOAA-21. In the case of M13, NOAA-21 consistently shows a smaller $d\tau/dz$ across all altitudes compared to S-NPP and NOAA-20. This indicates that in the M13 band, NOAA-21 experiences fewer extinction and larger transparency. Consequently, NOAA-21 is expected to observe higher TOA reflected radiance, resulting in higher BTs for M13.

Preprints.org (www.preprints.org) | NOT PEER-REVIEWED | Posted: 27 February 2024 doi:10.20944/preprints202402.1582.v1

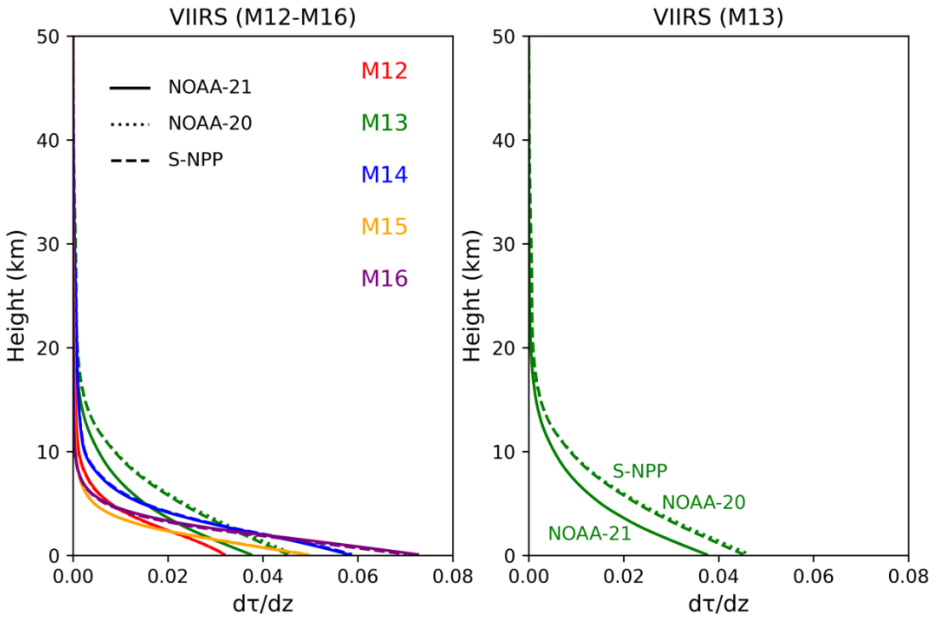

Figure 2. Weighting function profile of VIIRS TEB channels for S-NPP, NOAA-20, and NOAA-21, respectively. Where (a) shows all the channels and (b) shows only the M13 channel.

To further quantify the impact of the SRF differences among different VIIRS instruments, we conducted inter-comparisons of simulated Brightness Temperatures (BTs) relative to sea surface temperature (SST), as illustrated in Figure 3. This analysis combined the CRTM with the 1976 US standard atmosphere model. In the CRTM simulation setup, the only disparity across different VIIRS instruments arose from the difference in SRFs. Figure 3 clearly shows that the differences between the BTs (ΔBTs) among different VIIRS instruments do not exceed 0.5 K for all TEBs, except for M13. For M13, the ΔBTs between NOAA-21 and NOAA-20/S-NPP increase as SSTs rise. For example, when the SST is about 300K, both the differences $BT_{NOAA-21} - BT_{NOAA-20}$ and $BT_{NOAA-21} - BT_{S-NPP}$ reach around 3.0 K. This substantial discrepancy is primarily due to the notable SRF differences between NOAA-21 and NOAA-20/S-NPP, as illustrated in Figure 1. This also infers that measurements of fires on land would register higher temperatures on NOAA-21 compared to NOAA-20 and S-NPP.

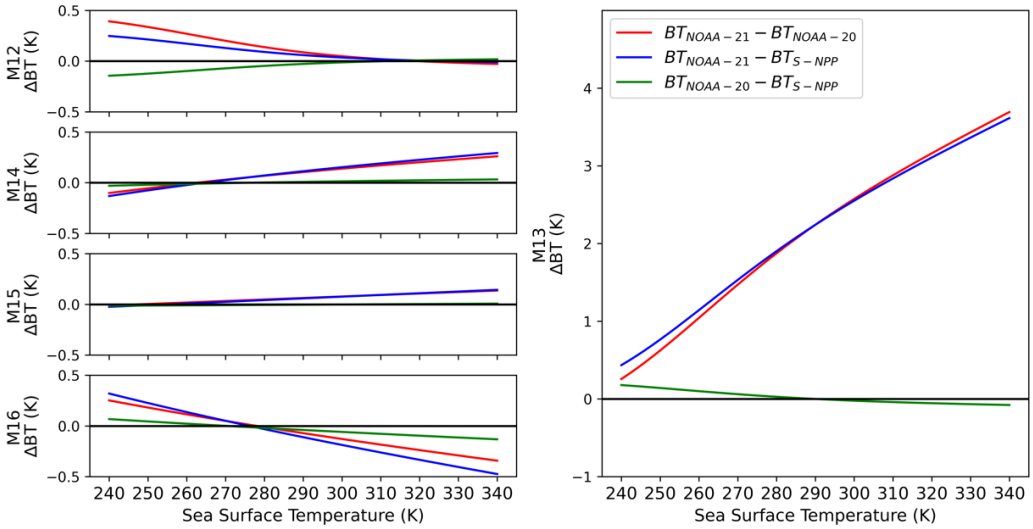

Figure 3. The differences of CRTM simulated BTs between different VIIRSs versus SSTs. The US1976 atmospheric profile has been used.

Preprints.org (www.preprints.org) | NOT PEER-REVIEWED | Posted: 27 February 2024 doi:10.20944/preprints202402.1582.v1

Above all, the establishment of a transfer reference that accounts for the spectral response differences among different VIIRS sensors is crucial for accurately assessing the inter-sensor consistency of VIIRS instruments.

2.2. CRTM Radiative Transfer Modeling

Following the methodology established by Liu et al. [21], this work adopts radiative transfer modeling (RTM) as the transfer reference. In this study, the CRTM (version 2.3), specifically designed for simulating Top-of-Atmosphere (TOA) satellite-measured radiance, was utilized for simulating VIIRS TEB BTs, alongside collocated VIIRS observations. The model can be downloaded from the Joint Center for Satellite Data Assimilation (JCSDA) at https://ftp.emc.ncep.noaa.gov/jcsda/CRTM/REL-2.3.0/. Quantitatively accounting for various factors, including Earth's surface reflection and radiation emission, single and multiple scattering, and gaseous absorption in the atmosphere [22], the CRTM also provides a comprehensive set of functions. These include forward modeling, adjoint modeling, tangent-linear modeling, and K-matrix modeling, catering to a wide range of modeling needs. As a rapid sensor-channel-based RTM tool, the CRTM has found widespread applications in the calibration, assimilation, and various remote sensing endeavors, encompassing data from shortwave, infrared and microwave sensor [24,25].

Figure 4 provides a visual representation of the configuration for CRTM simulations in this research. ECMWF global reanalysis data, which were processed every 6 hours with a spatial resolution of 0.25 degrees, served as essential inputs for CRTM modeling. These data include key parameters such as sea surface temperatures (SSTs), surface winds, and 37-level atmospheric profiles covering variables like water vapor, temperature, pressure, ozone, and more. The vertical profiles extended from the surface to about $1hPa$. To align ECMWF data with VIIRS observations, spatial and temporal interpolations were per-formed based on VIIRS observation time and locations. Additionally, the CRTM incorporated the Wu-Smith infrared water emissivity model for rough sea surfaces (Wu and

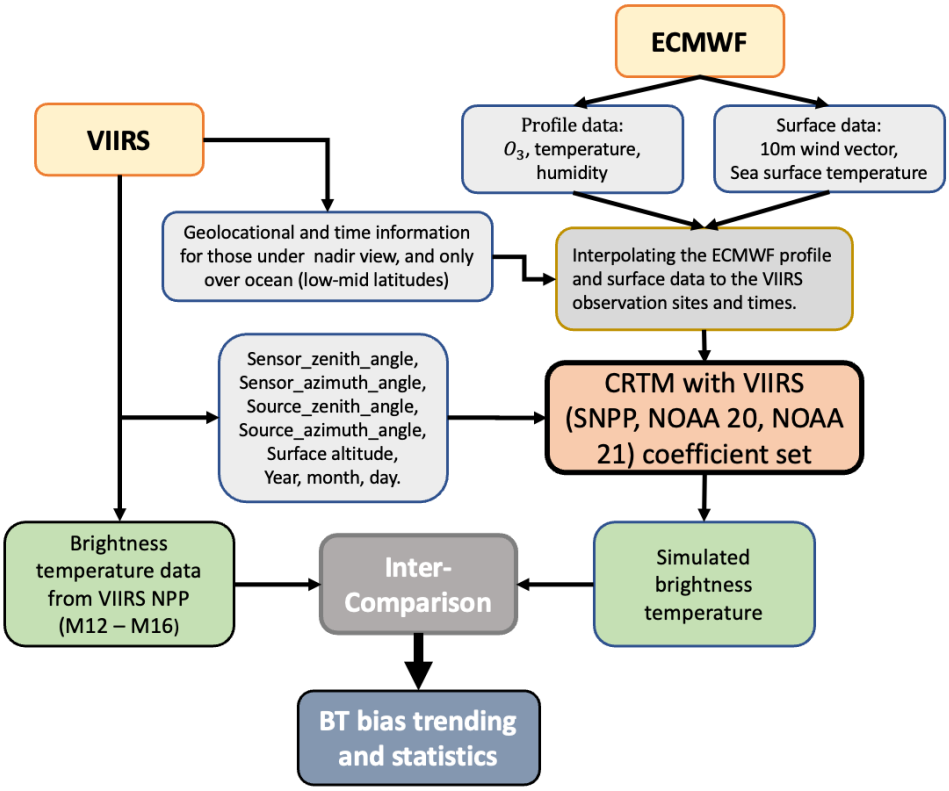

Figure 4. RTM simulation setup with CRTM as the simulator for long-term O-B difference evaluation of VIIRS TEBs.

 doi:10.20944/preprints202402.1582.v1

Smith 1997). This scheme calculates ocean surface emissivity, considering the view angle, frequency, and surface wind speed. Furthermore, to ensure the compatibility between CRTM and VIIRS, the availability of VIIRS-dependent spectral and transmittance coefficient files is necessary. The sensor-dependent transmittance coefficients are trained using a line-by-line radiative transfer model while considering the VIIRS spectral response function. This comprehensive approach guarantees the accurate replication of VIIRS TEBs' behaviors under specified conditions.

In this study, the assessments of VIIRS TEB stability and inter-sensor consistency are based on the comparisons of VIIRS measurements (O) with their co-located CRTM simulations, i.e., observation minus background BT differences (O-B ΔBTs).

2.3. Scene Target Selection

This research mainly focuses on warm target regions situated over ocean within the low to mid-latitudes from 60^oS to 60^oN. Areas with solar zenith angles falling within the range of 80 to 100 degrees are excluded to avoid the terminator region, where the angle between the sun and the satellite's line of sight is relatively high.

For each O-B BT difference comparison, approximately 100 VIIRS data points around the center of the target location at satellite nadir were collected. Over these 100 points, the mean and standard deviation of VIIRS pixel BTs were recorded. Subsequently, those VIIRS measurements affected by scene non-uniformity (standard deviation of $BT \geq 0.3$K) were removed. In addition, to mitigate the impact of cloud contamination, a straightforward yet effective cloud screen criterion was applied, removing any observations with absolute O-B BT difference equal to or exceeding 4 K across all VIIRS M TEBs. Further discussion regarding this cloud screening method will be presented in section 3.2.3. After the uniformity and cloud contamination screening, the O-B dataset typically contained about 30,000 to 50,000 valid data per day, ensuring the statistical robustness of the CRTM-based stability and consistency analysis. The ensemble of O-B BT differences over valid scenes during each day of interest was then utilized for comprehensive analyses, including mean O-B ΔBT calculations, mean double difference between different O-B ΔBT (referred to as O-O ΔBT), uncertainty assessments, and trending analyses. Collectively, these steps contribute to the thorough evaluation of VIIRS TEB stability and inter-sensor consistency.

2.4. Task Summary

This study conducts two distinct investigations with different time frames and objectives are conducted. Details are as follows:

1. Long-Term VIIRS stability evaluation (2012-2020):
- Objective: To assess the long-term stability of the NOAA STAR version 2 reprocessed S-NPP VIIRS M TEB data.
- Time Frame: February 2012 to August 2020.
- Data Collection: Monthly data from both S-NPP and ECMWF reanalysis were collected on the 15th day of each month during this timeframe.
- Methodology: Monthly O-B ΔBT calculations were analyzed.
2. Inter-VIIRS data consistency analysis (since Mar. 18, 2023):
- Objective: To analyze the inter-sensor consistency of M-TEB data across three VIIRS instruments: S-NPP, NOAA-20, and NOAA-21, each named after the satellite it is aboard.
- Time Frame: March 18, 2023, to Nov. 30, 2023.
- Data Collection: Daily data from S-NPP/NOAA-21/NOAA-20, and 6-hour ECMWF reanalysis data were collected during this period.
- Methodology: Daily calculations of both O-B ΔBTs and double difference (O-O) ΔBTs were conducted.

The choice to conclude task 1 in 2020 and set the endpoint for task 2 in November 2023 was primarily influenced by the availability of VIIRS TEB data when this research was conducted.

3. Results

 doi:10.20944/preprints202402.1582.v1

3.1. Long-Term Satbility of VIIRS S-NPP M TEBs

3.1.1. Analyses on the Long-Term Time Series

Figure 5 illustrates the long-term time series spanning from February 2012 to August 2020, displaying the O-B BT differences (O-B ΔBTs) between VIIRS observed (O) and CRTM modeled (B) for VIIRS S-NPP M-band TEBs (M12 – M16). The figure also includes error bars representing uncertainties (blue vertical bar) and trend lines (red). The time series in Figure 5 reveals that the daily mean O-B ΔBTs for VIIRS M TEBs remain stable and consistent with ECMWF reanalysis data over the specified period. Except for M12, the mean O-B differences are all less than 0.26 K, with standard deviations $\leq 0.06K$, closely aligning with the 0.2 K BT difference between VIIRS and MODIS reported in prior

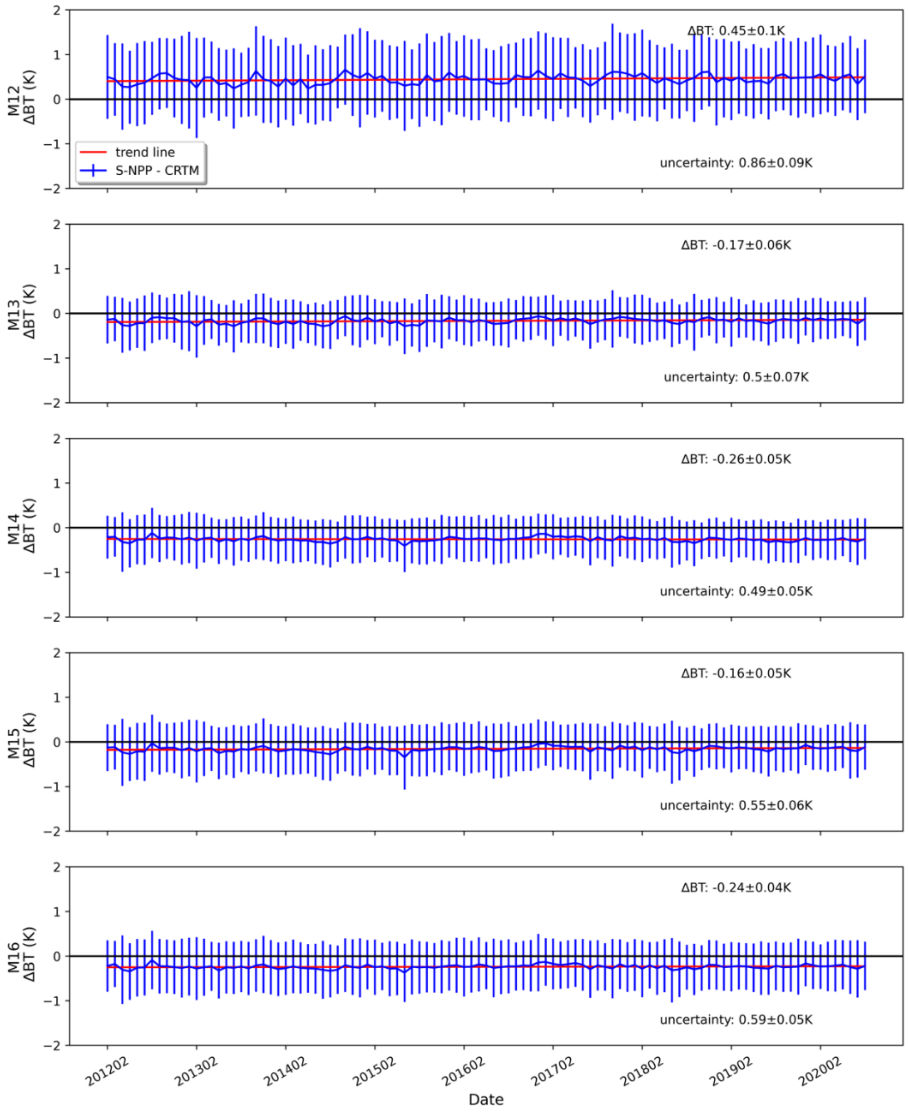

Figure 5. Long-term monthly trending of O-B ΔBT between VIIRS observed (O) and CRTM modeled (B) (blue) for VIIRS S-NPP M TEBs along with their uncertainties (1σ, and σ the standard deviation, bars) and trend lines (in red) from 201202 to 202008. The numbers shown here are the long-term means of monthly ΔBT with their standard deviations, along with those for uncertainties.

studies [8–12]. For M12, the long-term mean O-B differences exhibit largest values of $0.45 \pm 0.1K$, along with the highest uncertainty at 0.86 K, compared to the other M TEBs.

To gain a deeper insight into the distinctive behavior of M12, we conducted a detailed analysis, specifically separating its O-B ΔBTs during daytime and nighttime. In this study, we classified daytime and nighttime measurements based on the solar zenith angle (SZA) as follows:

 doi:10.20944/preprints202402.1582.v1

$$\begin{matrix} SZA < & 80^o, & daytime \\ SZA > 100^o, & & Nighttime' \end{matrix} \quad (2)$$

Figure 6 depicts the long-term O-B ΔBTs for M12 during daytime and nighttime, respectively. Particularly noteworthy is the observation that in M12, the long-term mean of O-B differences during daytime is significantly larger than that during nighttime, with values of $0.81 \pm 0.16\,K$ and $0.11 \pm 0.08\,K$, respectively. Additionally, the long-term mean uncertainty during daytime for M12 reaches 0.91 K, surpassing its nighttime uncertainty of 0.62 K. Clearly, the unique behavior of M12 primarily stems from its daytime measurements, which were contaminated by solar contributions. The M12 operates as a partial shortwave channel. The solar contribution through sea surface reflection to TOA radiances is particularly notable during the daytime [24]. Consequently, the uncertainty stemming from the ocean bidirectional reflectance distribution function (BRDF) calculation results in a more pronounced CRTM simulation uncertainty for M12 over daytime than over nighttime. Hence, in the RTM-based TEB quality evaluation method, challenges arise from the intricacies and uncertainties inherent in the RTM simulation setup, including those associated with modeling surface emissivity and reflectivity.

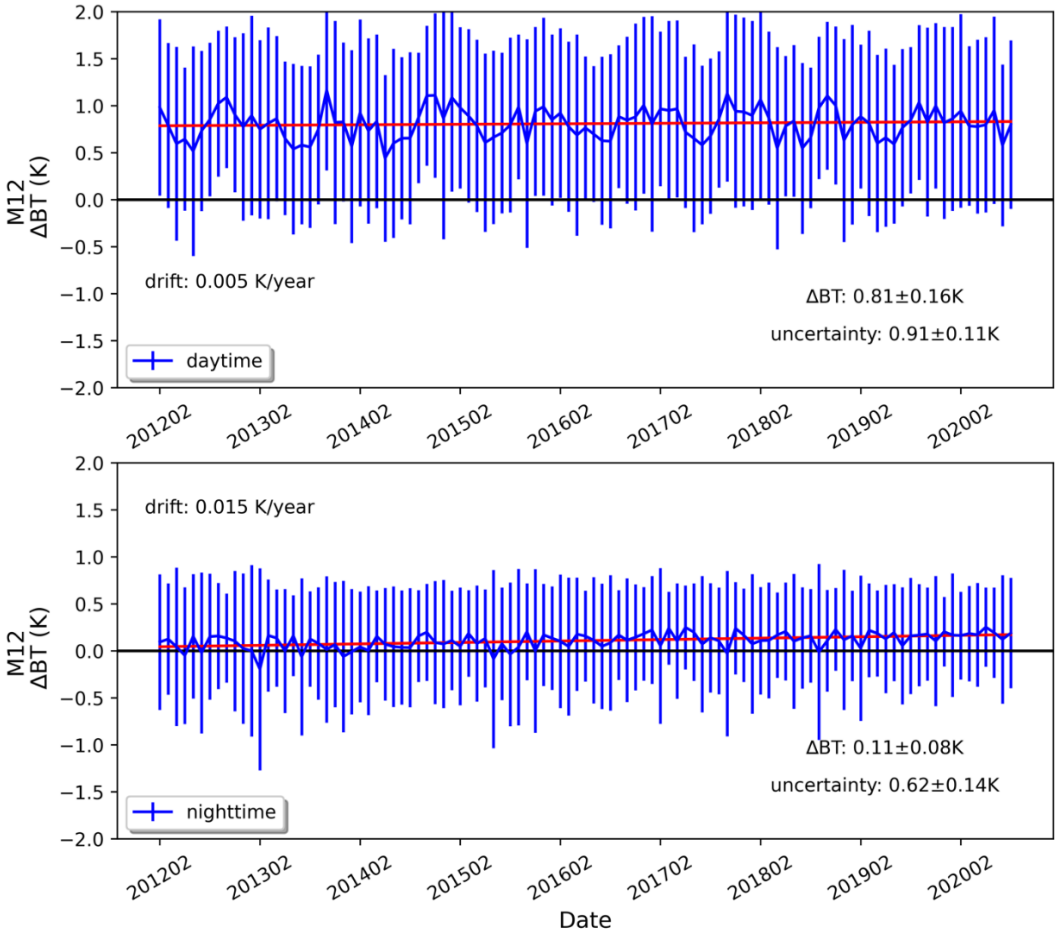

Figure 6. The same as Figure 5, except for M12 during daytime and nighttime, respectively.

3.1.2. Analysis on O-B BT differences against scene temperature

Figure **7** portrays O-B BT differences against scene temperature, offering valuable insights into the behavior of the S-NPP VIIRS TEBs. In this figure, the shaded depicts 2-dimension O-B ΔBT distribution densities in unit K^{-2}, derived using O-B BT differences and S-NPP VIIRS BT observations during 2012.02 to 2020.08. About 61.0% to 76.9% of the scene BTs fall within the range of 290 K and above, emphasizing the prevalence of warm scene targets in this study. In Figure **7,** a significant concentration of distribution density is revealed within the scene temperature range of 290 to 300 K for each M TEB. In this range, about 67%, 89%, 84%, 83% and 77% of ΔBTs have values no more than

 doi:10.20944/preprints202402.1582.v1

0.6 K for M12 – M16, respectively. Further examining the mean O-B ΔBTs versus scene temperature in Figure **7** demonstrates no significant scene temperature dependencies for the O-B differences of M14 to M16. However, for M13, the mean O-B BT bias curve comprises a low-temperature segment marked by insignificant temperature dependence and a high-temperature segment (above 300 K) characterized by a downward trend with increased scene temperature. Only about 1% of BTs for M13 are above 300 K. Therefore, the downward trend in the high-temperature segment for M13 maybe be caused by the data under-sampling. For M12, it displays a noticeable overall upward trend in the mean O-B ΔBT curve

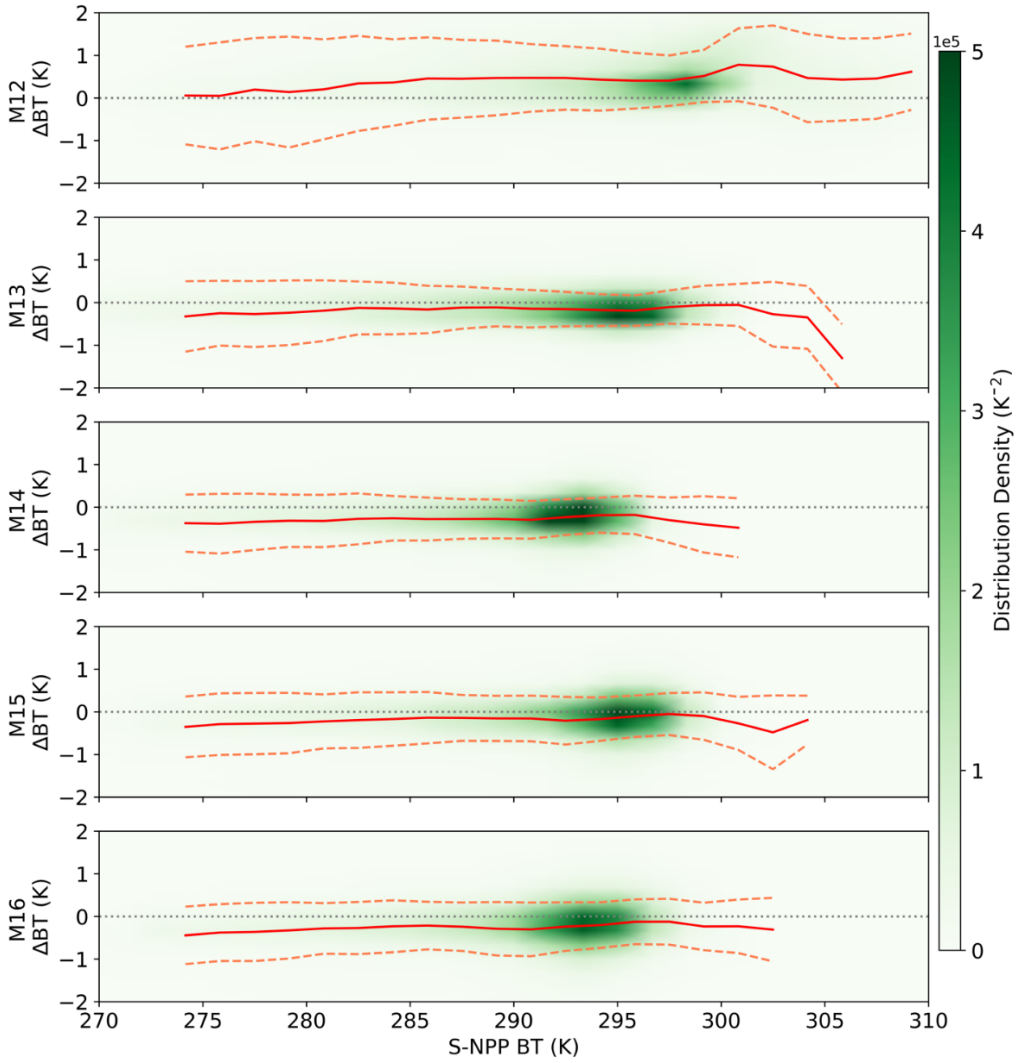

Figure 7. The dependence and distribution of O-B BT difference with respect to the BT measurement of S-NPP for M12-M16 TEBs. The O-B distribution statistics are derived using O-B BT difference and S-NPP VIIRS observations from 2012 to 2020. The curves overlayed with the distribution density plot show the mean (red solid) and one standard deviation from the mean (red dashed) of O-B BT differences in each BT bin.

as the scene temperature increases, especially below 302 K. Above 302 K, where less than 1% of BTs fall within this range, the unusual performance of M12, characterized by a downward and then upward trend, suggests a potential association with data under-sampling. To better understand the distinct behavior of M12 when scene temperature below 302 K—higher scene temperatures correspond to higher ΔBTs—we have further investigated the disparities between its daytime and nighttime observations. Figure 8, a counterpart to Figure 7, narrows its focus exclusively on S-NPP VIIRS M12 with a deliberate separation of daytime and nighttime data. The findings from Figure 8 reveal that during the day, ΔBTs for M12 are consistently large and stable, around 1 K across the

 doi:10.20944/preprints202402.1582.v1

whole BT range from 270 to 302 K. This is primarily attributed to solar contributions, as discussed above. Conversely, during the night, a notable upward trend appears with increasing BTs, characterized by negative ΔBTs at lower temperatures (< about 287 K) and positive ΔBTs at higher temperatures (> about 287 K). Hence, the distinctive behavior of the M12 mainly results from the combined influence of daytime and nighttime measurements. These observations enhance our understanding of the temperature dependence of O-B differences within the context of S-NPP VIIRS TEBs, emphasizing the diurnal variations of O-B ΔBTs.

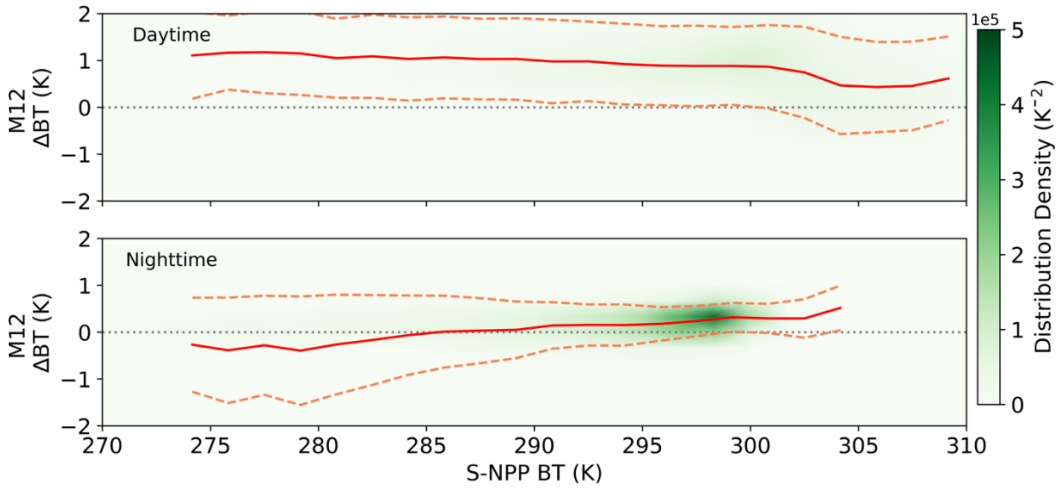

Figure 8. The same as **Figure 7,** but exclusively on the S-NPP VIIRS M12 with daytime and nighttime data separated.

3.1.3. Analysis on the drifts of O-B BT differences from 2012 to 2020

Next, our focus will shift to evaluating the long-term stability of VIIRS S-NPP TEBs through the O-B difference analysis. The long-term time series of O-B BT differences are further analyzed using linear regression to calculate the yearly BT drift rate for each S-NPP TEB. The results of this analysis are presented in Table 2, along with the correspond- ing 95% confidence interval (CI), providing a quantitative means to evaluate the stability

Table 2. Averaged yearly BT drifts ±95%CI (K/year) of VIIRS NPP TEBs (M12 – M16) derived from O-B analysis with CRTM simulations. ΔBT is the O-B BT difference, here O represents the VIIRS NPP observed BTs, and B represents the CRTM simulated BTs.

VIIRS TEBs	Central wavelength (*μm*)	Averaged yearly BT drift ± 95%CI (K/year)
M12	3.693	0.0102±0.0076
M13	4.065	0.0061±0.0043
M14	8.577	-0.0016±0.0037
M15	10.710	0.0049±0.0040
M16	11.832	0.0028±0.0035

of VIIRS S-NPP TEBs. Our results clearly show that VIIRS S-NPP TEBs exhibit radiometric stability, with the average yearly O-B ΔBT drift being less than 0.0061 K/year for M13 – M16, and slightly higher at 0.0102 K/year for M12. As shown in Figure 6, for M12, the yearly drifts for daytime and nighttime are 0.005 K/year and 0.015 K/year, respectively.

This highlights that the higher M12 yearly drift shown in Table 2 primarily stems from its nighttime data, which is not influenced by the large uncertainty from the solar contribution. This aspect deserves our attention in future VIIRS calibrations.

Cao et al. (2021) conducted a comparative analysis of S-NPP VIIRS BTs and those acquired from the co-located Cross-track Infrared Sounder (CrIS) [7]. Their investigation revealed trends in the VIIRS-CrIS BT difference of about -0.003, -0.002, and -0.002 K/year for M13, and M15-M16,

 doi:10.20944/preprints202402.1582.v1

respectively. Here, utilizing the CRTM modeling as the transfer, we obtained slightly higher corresponding drifts for these three TEBs, with values of about 0.0061, 0.0049, and 0.0028 K/year, respectively. Despite identifying of larger drifts in our study, the consistent discovery of similar magnitudes on the order of 10^{-3} aligns with the findings of Cao et al. [7]. Moreover, abnormal satellite movements, like jiggers, can impact satellite observation quality. The co-location of CrIS and VIIRS on the same satellite suggests that they experience similar noises resulting from the same unexpected satellite movements. As a result, while smaller BT differences are observed, anomalies arising from these movements cannot be addressed solely by comparing co-located VIIRS and CrIS data. This emphasizes the importance of introducing an independent method, such as the RTM modeling method, to evaluate the VIIRS performances alongside the co-located instrument comparisons. In addition, the RTM method is applied across all M TEBs (M12 – M16) without imposing any spectral constraints. In contrast, Cao et al. [7] only evaluated three M bands (M13, M15, M16) comparing VIIRS and CrIS data. Undoubtedly, further information about the remaining two bands has been unveiled through using the RTM method.

Moreover, Zou et al. [26] demonstrated the high radiometric stability performance of U.S. satellite microwave sounders, noting a trend within 0.04 K/decade in the measured atmospheric temperature as indicative of reliable climate change detection. Our analyses, in Table 2, reveal drifts of about 0.016 and 0.028 K/decade for S-NPP VIIRS M14 and M16, respectively, below 0.04 K/decade. This demonstrates that the reliability of observations from M14 and M16, making them suitable for climate change studies. While M15 exhibits a trend of about 0.049 K/decade, it may still be considered suitable for such studies.

Our independent analysis reaffirms the overall stability of VIIRS S-NPP TEBs over ocean surfaces, particularly warm targets.

3.2. Inter-sensor Consistency of VIIRS M TEBs

As of February 2023, three VIIRS instruments onboard S-NPP, NOAA-20, and NOAA-21 have been operating steadily. Considering there are various events before March 17, such as mid-mission outgassing (MMOG) from February 23 to February 25, OBC BB WUCDs from March 10 to March 13 and from March 16 to March 18, which affected the quality of VIIRS TEBs' observations, we have limited our analysis to data collected after March 17 to calculate the means of BT differences, their standard deviations and other variables.

3.2.1. Analyses of the time series from March 18 to November 30, 2023

In Figure 9, the daily trends of O-B BT differences in 2023 are presented, for VIIRS TEBs on NOAA-21, NOAA-20 and S-NPP. The gaps in data on February 24, March 12, March 13 and May 4th indicate instances where data were missing due to VIIRS TEB post-launch calibration events mentioned above. As shown in Figure 9, across all the M TEBs and the three VIIRS instruments on different satellites, the averaged O-B differences consistently stay below 0.46 K, with standard deviations not larger than approximately

 doi:10.20944/preprints202402.1582.v1

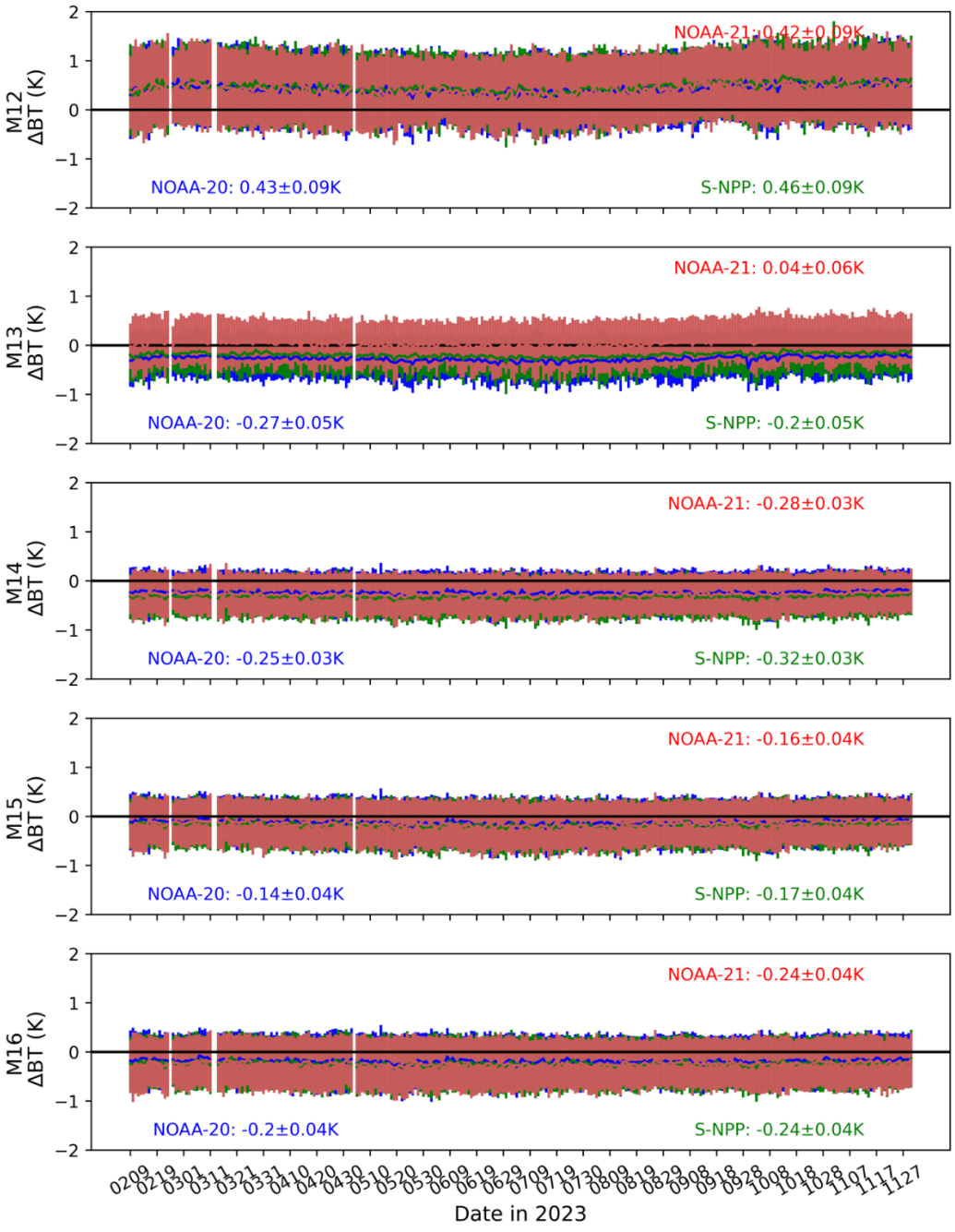

Figure 9. Daily trending of O-B ΔBTs (solid) and their uncertainties (bars) for VIIRS S-NPP (green), NOAA-20 (blue), and NOAA-21 (red) TEBs (M12 – M16). The numbers shown in each band are temporal means of daily ΔBT ± their standard deviations.

0.09 K. These values are comparable to those present in the long-term monthly trending of SNPP VIIRS O-B ΔBTs shown in Figure 5. When disregarding the signs, for M12, all three VIIRS instruments show comparable largest averaged O-B ΔBTs among all M TEBs, near 0.43 K, while for M14 to M16, they exhibit similar small, averaged O-B ΔBTs, not exceeding about 0.32, 0.17, and 0.24 K, respectively. In the case of M13, the mean O-B ΔBT for NOAA-21 is only 0.04 K, while for NOAA-20 and S-NPP, it is -0.27 K and -0.20 K, respectively. The significant discrepancy between NOAA-21 and NOAA-20/S-NPP in M13 is attributed to the substantial differences in their SRFs, as illustrated in Figure 1b. Certainly, even with CRTM as the reference, the non-linear atmospheric absorption effects resulting from variations in the SRF cannot be entirely removed. Notably, M12 consistently displays the largest O-B ΔBTs among all the TEBs for all VIIRS instruments, predominantly due to the

 doi:10.20944/preprints202402.1582.v1

shortwave solar contributions. In addition, the bars illustrated in this figure represent uncertainties, primarily arising from the complexities and uncertainties in the RTM simulation setup, as discussed previously.

To better evaluate the inter-sensor consistency among different VIIRS instruments, we further conducted double-difference analyses by subtracting any pair of O-B ΔBT values between S-NPP, NOAA-20, and NOAA-21 to derive inter-sensor VIIRS O-O ΔBTs. Figure 10 shows the daily means of O-O ΔBTs between different pairs among these three VIIRS instruments. The numbers displayed in each band represent the temporal means of daily O-O ΔBT±standard deviations. Our findings reveal that, for all moderate-resolution VIIRS TEBs (excluding M13), the means of inter-VIIRS BT differences consistently remain below 0.08 K. These values are 1-2 orders of magnitude smaller than those of O-B ΔBTs

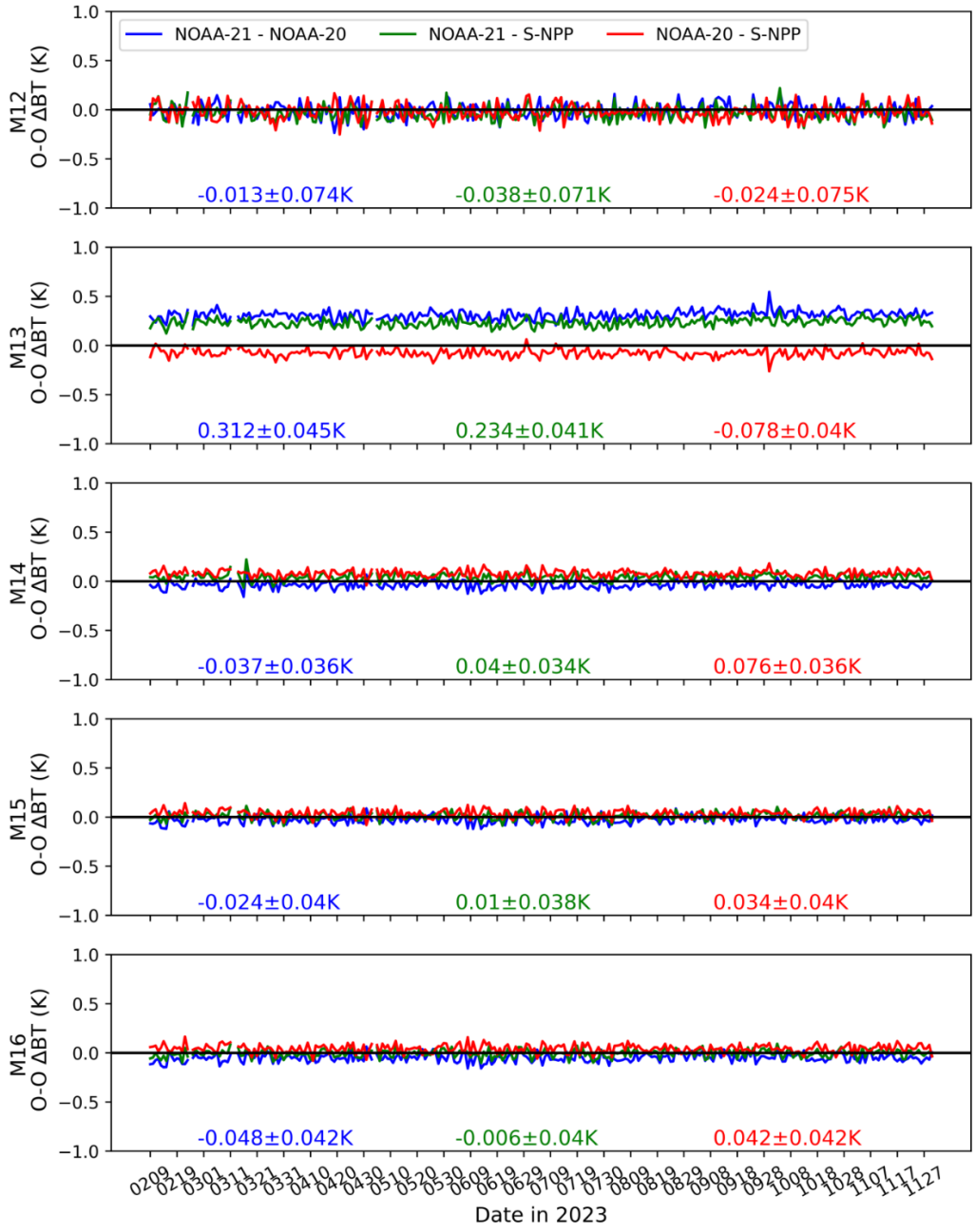

Figure 10. Comparisons of O-O ΔBTs between different pairs among S-NPP/NOAA-20/NOAA-21. The numbers show in each band are temporal means of daily O-O ΔBT±standard deviations.

 doi:10.20944/preprints202402.1582.v1

shown in Figure 9, even for M12. Specifically, for M12, the O-O $\overline{\Delta BT}s$, with values of 0.013 K and 0.024 K for NOAA21 – NOAA-20 and NOAA-20 – S-NPP, respectively, stand out as the smallest among all M TEBs, while the NOAA-21 – NOAA-20 value of -0.038 K falls within the range of the other bands, except for M13. This demonstrates that the double-difference approach mitigated uncertainties and biases inherent to CRTM simulations, including those originating from solar contributions in M12, establishing a robust mechanism for assessing inter-sensor VIIRS consistency. For M13, the SRF of NOAA-21 significantly differs from those of NOAA-20 and S-NPP. That leads to inter-VIIRS BT differences between NOAA-21 and NOAA-20/S-NPP are about 0.312 and 0.234 K, respectively, which are 1-2 orders of magnitude larger than those in the other bands, but still comparable to the 0.2 K difference between VIIRS and MODIS.

Figure 11 directly compares the temporal means of O-O ΔBTs (K) among these three VIIRS instruments for each M TEB in bar plots. Clearly, the O-O ΔBTs among different VIIRS instruments exhibit different performances for different bands. For example, for M15 and M16, the averaged O-O ΔBTs are smallest between NOAA-21 and S-NPP, while in M12 and M14, the best consistency can be found between NOAA-21 and NOAA-20.

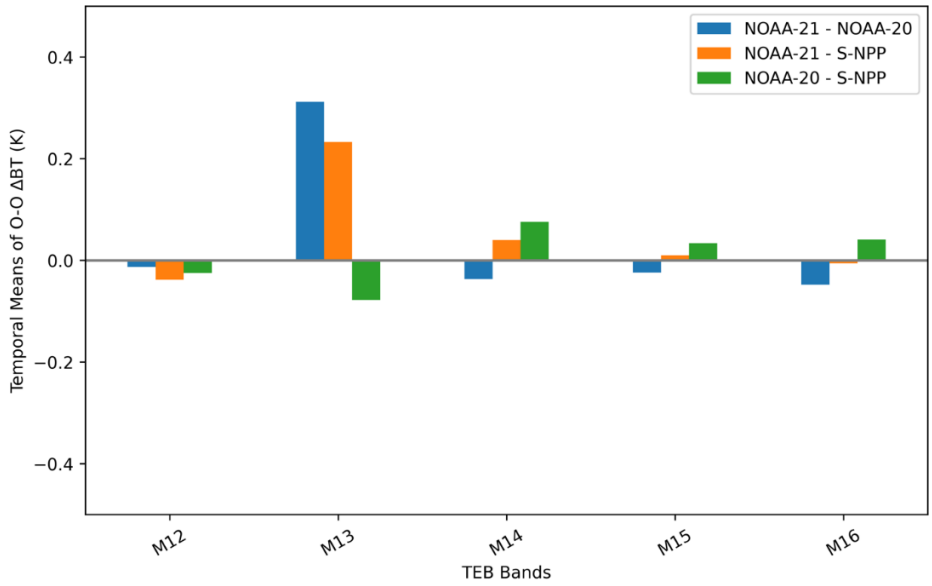

Figure 11. Comparisons of the temporal means of O-O ΔBTs (K) among S-NPP/NOAA-20/NOAA-21 in bar plots.

Furthermore, for better comparisons, all temporal averaged O-B and O-O ΔBTs along with their standard deviations for these three VIIRS instruments are also summarized in Table 3 and Table 4.

Table 3. Temporal mean of daily averaged O-B ΔBTs (K) along with their standard deviations for NOAA-21, NOAA-20, and S-NPP VIIRS TEBs.

VIIRS TEBs	O-B $\overline{\Delta BT}\pm\sigma$ (K) ($\overline{\Delta BT}$: Temporal mean of daily mean ΔBT; σ: standard deviation)		
	NOAA-21	NOAA-20	S-NPP
M12	0.42±0.09	0.43±0.09	0.46±0.09
M13	0.04±0.06	-0.27±0.05	-0.20±0.05
M14	-0.28±0.03	-0.25±0.03	-0.32±0.03
M15	-0.16±0.04	-0.14±0.04	-0.17±0.04
M16	-0.24±0.04	-0.20±0.04	-0.24±0.04

Table 4. Temporal mean of daily averaged O-O ΔBTs (K) along with their standard deviations for NOAA-21, NOAA-20, and S-NPP VIIRS TEBs.

 doi:10.20944/preprints202402.1582.v1

VIIRS TEBs	O-O $\overline{\Delta BT}\pm\sigma$ (K) ($\overline{\Delta BT}$: Temporal mean of daily mean ΔBT; σ: standard deviation)		
	NOAA-21 – NOAA-20	NOAA-21 – NOAA-20	NOAA-20 – S-NPP
M12	-0.013±0.074	-0.038±0.071	-0.024±0.075
M13	0.312±0.045	0.234±0.041	-0.078±0.040
M14	-0.037±0.036	0.040±0.034	0.076±0.036
M15	-0.024±0.040	0.01±0.038	0.034±0.040
M16	-0.048±0.042	-0.006±0.040	0.042±0.042

3.2.2. Analyses on the relationship between ΔBTs and scene temperatures

As we know, VIIRS calibration biases usually depend on scene temperatures. Therefore, Figure 12 presents (a) the relationship between O-B ΔBTs and sea surface temperatures (SST) and (b) the relationship between O-O ΔBTs and SST. The SST covers a range from 272 to 305 K, divided into 33 bins, each with a width of 1 K. Since this study focuses on warm temperature targets, this SST range effectively covers most of the cases. From this figure, we observe clear increases in O-B ΔBTs as SSTs rise, especially when SST is below 300 K across all M TEBs. However, no apparent dependencies of O-O ΔBT on SST are observed for all TEBs except for M13. For these TEBs, the O-O ΔBTs consistently hover

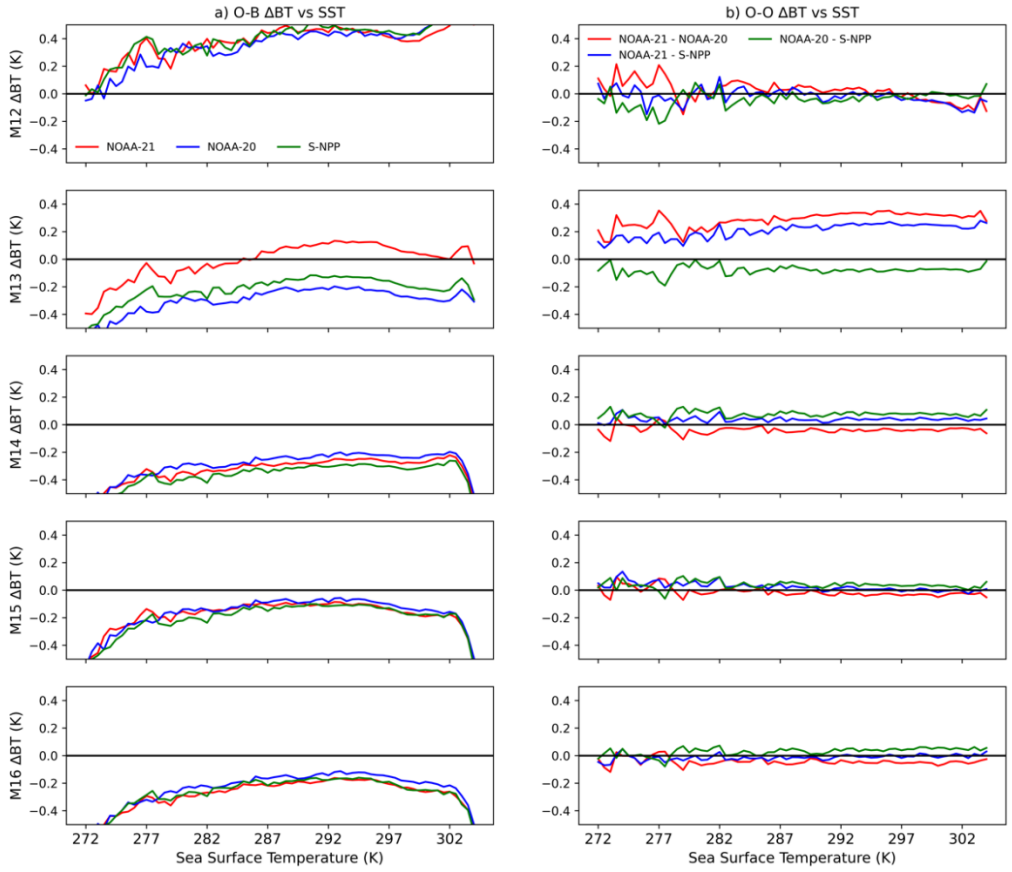

Figure 12. (a) the relationship between O-B ΔBTs and SSTs; (b) the relationship between O-O ΔBTs and SSTs. The SSTs covers a range from 272 to 305 K, which is divided into 33 bins, each with a width of 1 K.

close to zero, significantly smaller than the corresponding O-B ΔBTs. Evidently, the double difference method successfully alleviating the inherent uncertainties and biases associated with CRTM simulations. While for M13, due to the SRF differences, the O-O ΔBTs between NOAA-21 and

Preprints.org (www.preprints.org) | NOT PEER-REVIEWED | Posted: 27 February 2024 doi:10.20944/preprints202402.1582.v1

NOAA-20/S-NPP are around 0.2 K. This deviation is evident, deviating from zero, yet it remains comparable to the 0.2 K difference between VIIRS and MODIS.

In Figure 3, the rates of increase in the direct O-O BT differences between NOAA-21 and others with rising SSTs reach about 0.035 K/K, mainly due to substantial differences in their SRFs. However, the double difference method significantly mitigates this false large upward trend for M13. As shown in Figure 12, the slope of O-O ΔBTs between NOAA-21 and NOAA-20/S-NPP with rising SSTs consistently stay below 0.0033 K/K, an order of magnitude smaller than the corresponding rates in the direct O-O BT comparisons. This highlights the effectiveness of the double difference approach in minimizing the influence of SRF differences when assessing inter-sensor consistency.

3.2.3. Analyses on the spatial variation of O-O ΔBTs

In this study, we have further analyzed the geographical distributions of the O-O ΔBTs, considering grids with resolution of $2^o \times 2^o$. The O-O ΔBT values have been aggregated within each grid, and their respective grid-means are presented in Figure 13, showcasing comparisons between (a) NOAA-21 versus NOAA-20, (b) NOAA-21 versus S-NPP, and (c) NOAA-20 versus S-NPP, respectively. From this figure, the O-O grid-mean ΔBTs exhibit similar spatial distributions among (a), (b) and (c) in each TEB, except for M13. In (a) and (b) for M13, warm colors (red) dominate most ocean areas, especially within $40^oS\ to\ 40^oN$. This indicates that NOAA-21 measurements consistently register higher BTs compared to both NOAA-20 and S-NPP, which is mainly attributed to the smallest

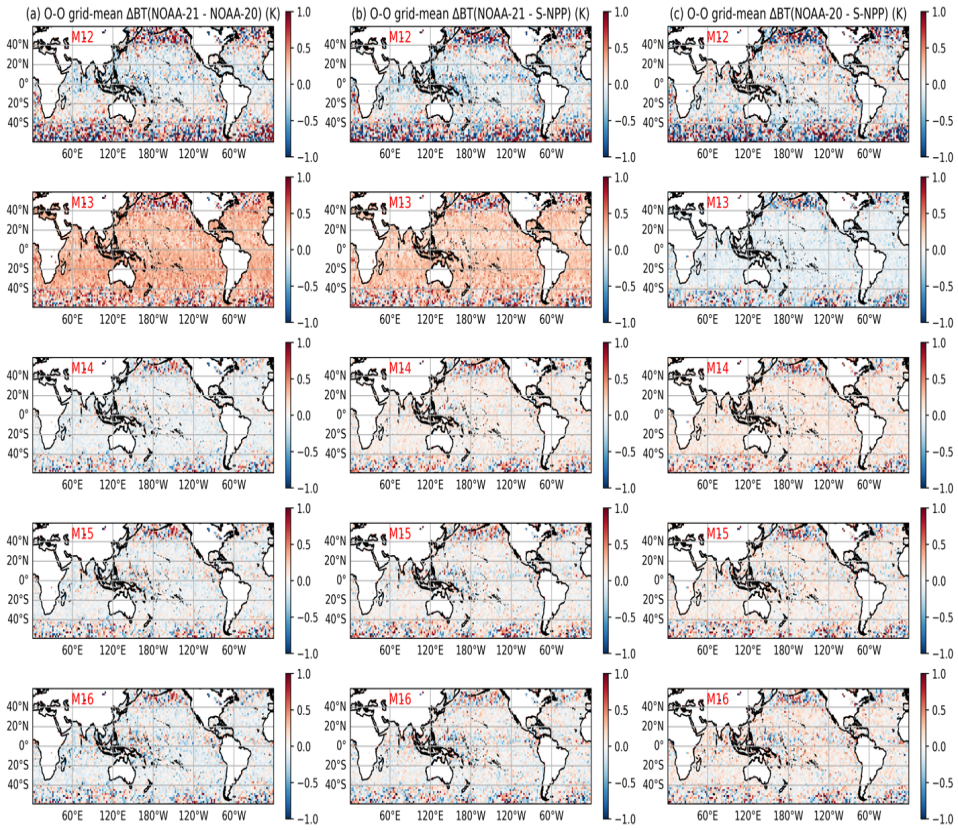

Figure 13. Longitude-Latitude distributions of grid-mean O-O ΔBTs for (a) NOAA-21 – NOAA-20, (b) NOAA-21 – S-NPP, and (c) NOAA-20 – S-NPP, respectively.

weighting function of NOAA-21 (Figure 2). In addition, apart from M13, M12 consistently displays larger spatial variations than the other TEBs. This mainly results from solar contribution through the ocean reflection during the daytime, as discussed earlier. Moreover, in general, the grid-mean O-O ΔBTs are very small for all TEBs, typically falling within the range of -0.2 to 0.2 K. This demonstrates the effectiveness of our cloud screening method, wherein any observations with an

 doi:10.20944/preprints202402.1582.v1

absolute O-B BT difference equal to or exceeding 4 K across all VIIRS M TEBs have been removed. However, we still observe the presence of O-O ΔBTs over the Intertropical Convergence Zone (ITCZ) for M15 and M16, suggesting that our cloud screening method may not entirely remove certain types of clouds, such as cirrus clouds. Cirrus clouds are high-level clouds with semi-transparent characteristics, leading to O-B ΔBT values below 4 K. Therefore, further analyses, for example, adjustments to cloud screening thresholds, especially for cirrus, should be considered.

Figure 14 illustrates the longitude-latitude distributions of grid-mean O-O ΔBTs for (a) daytime and (b) nighttime specifically for O-O between NOAA-21 and NOAA-20. Similar spatial distributions are observed for NOAA-21 versus S-NPP and NOAA-20 versus S-NPP for both daytime and nighttime for all TEBs (not shown). Except for M12, the spatial distributions of grid-mean O-O ΔBTs for all other M TEBs remain consistent, particularly evident between 40^oS and 40^oN, during both daytime and nighttime. For M12, the contrast is evident as the values of O-O ΔBTs during daytime (Figure 14a) are notably higher than those during nighttime (Figure 14b), offering evidence of solar contribution in M12 during daytime even after employing the double-difference method for mitigation. Furthermore, quite large values of O-O ΔBTs exist in high latitudes ($> 40^o$) during the night**.** For M12, this is partially due to the solar contamination. In this study, the classification of daytime and nighttime measurements relies on the solar zenith angle (SZA)

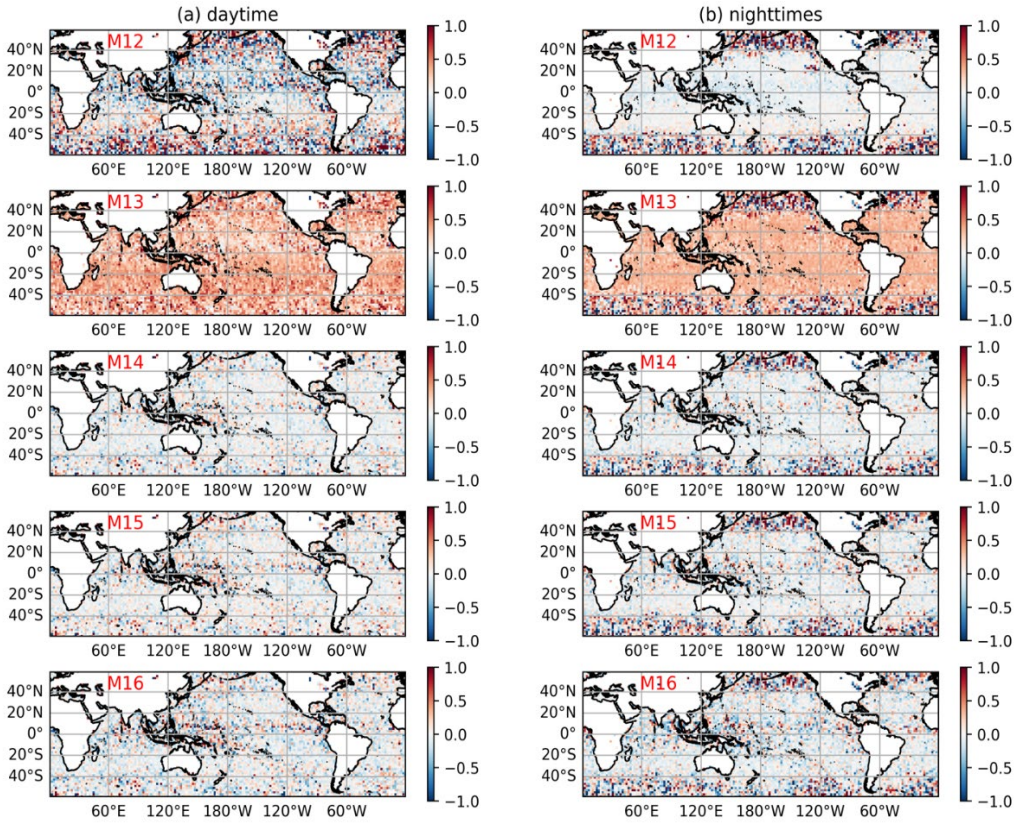

Figure 14. Longitude-Latitude distributions of grid-mean O-O ΔBTs for (a) daytime and (b) nighttime for NOAA-21 – NOAA-20.

determined by formula (2). Therefore, at high latitudes, solar contribution may still exist even when SZA exceeds 100^o. However, further research is needed to understand this phenomenon for the remaining M TEBs, given that they are not operated in solar bands.

The RTM-based approach effectively demonstrates the excellent inter-sensor consistency of VIIRS TEBs, even in the M13 band. Using the CRTM simulation as the transfer reference, this study offers a comprehensive quality evaluation of VIIRS TEB data to ensure consistency among S-NPP, NOAA-20, and NOAA-21.

 doi:10.20944/preprints202402.1582.v1

4. Conclusions

This work employs radiative transfer modeling as the transfer reference. The Community Radiative Transfer Model (CRTM) is applied to simulate VIIRS TEB BTs using ECMWF reanalysis data as inputs for the collocated VIIRS observations. All analyses in this paper are confined to the clear-sky ocean surface between 60^oS and 60^oN as the areas of interest. Two significant investigations with different time scales have been conducted. The first study evaluates the long-term (2012-2020) stability of S-NPP VIIRS TEBs using the NOAA STAR version 2 reprocessed S-NPP VIIRS moderate-resolution (M12-M16) TEBs data, based on the observation minus background BT differences between VIIRS measurements (O) and CRTM simulations (B). The second study focuses on assessing the inter-sensor VIIRS TEB data consistency among S-NPP, NOAA-20, and NOAA-21 over eight months from March 18, 2023 to November 30, 2023, as revealed through the double-difference analysis method. This method is carried out by subtracting any pair of O-B BT differences among the three satellites.

We have found that firstly, there is robust long-term stability observed in S-NPP VIIRS TEBs. The drifts of the O-B BT differences are consistently found to be less than 0.105 K/Decade for S-NPP VIIRS bands M12-M16. M14 and M16 measurements can be reliably utilized for climate change studies due to their drifts below 0.04 K/Decade. Secondly, excellent inter-sensor consistency is observed among different VIIRS instruments. For all moderate-resolution VIIRS TEBs (excluding the M13), the means of inter-VIIRS BT differences consistently have values < 0.08 K. In the case of M13, the Spectral Response Function of NOAA-21 is significantly different from those of NOAA-20 and S-NPP. As a result, the inter-VIIRS BT differences between NOAA-21 and NOAA-20/S-NPP have values of about 0.234 to 0.312 K, respectively. These BT differences are still comparable to the 0.2 K difference between VIIRS and MODIS.

In conclusion, our study demonstrates that the RTM-based TEB quality evaluation method is robust and versatile, assessing both long-term sensor stability and inter-sensor consistency. By employing CRTM simulation as the transfer reference, we provide a comprehensive quality evaluation of VIIRS TEB data, ensuring the stability of S-NPP VIIRS and the consistency among S-NPP, NOAA-20, and NOAA-21. Furthermore, the double-difference approach mitigates uncertainties and biases inherent to CRTM simulations and further minimizing the influence of SRF differences, establishing a robust mechanism for assessing inter-sensor consistency. These findings are meaningful, as the stability and consistency of VIIRS TEBs, the focal points of this study, are crucial for maintaining and upholding the data quality of downstream VIIRS EDR products and advancing Earth science research and climate applications.

Based on the results of this study, several discussions arise. Firstly, significant differences in the SRFs among NOAA-21, NOAA-20, and S-NPP VIIRS instruments are noted for M13. While using CRTM as the transfer reference mitigates these SRF differences to a considerable extent, it's essential to acknowledge that its non-linear effects cannot be entirely removed. Secondly, except for M13, M12 consistently exhibits greater spatial variations of O-O ΔBTs compared to the remaining TEBs. In M12, the influence of solar contribution through sea surface reflection to the TOA radiance during the day should not be underestimated even after employing the double-difference method for mitigation. Thirdly, at high latitudes in both the northern and southern hemispheres, there's a possibility of sunlight contamination in the M12 nighttime measurements, even when the SZA exceeds 100^o. However, further research is needed to understand the similar phenomenon for the remaining M TEBs, given that they are not operated in solar bands. Fourthly, while the cloud screening method employed in this study is effective, it may not remove all observations contaminated by clouds, such as those associated with cirrus clouds. As a result, further investigations, including adjusting cloud screening thresholds, should be conducted. Furthermore, it is crucial to highlight the noticeable positive yearly drift of approximately 0.015 K/year in S-NPP M12 during the night. This trend necessitates careful consideration in future VIIRS calibrations.

Author Contributions: Conceptualization, F.Z., X.S. and C.C.; methodology, F.Z., X.J., T-.C.L. and X.S.; software, F.Z., Y.C., X.J. and T.-C.L.; validation, F.Z.., X.S., W. W., and Y.C.; formal analysis, F.Z., W.W. and X.S.; investigation, F.Z., X.S. and Y.C.; resources, C.C., X.S. and Y.C.; writing—original draft preparation, F.Z.;

writing—review and editing, F.Z., X.S., C.C., Y. C., W.W., T.-C.L., and X. J. ; visualization, F.Z.; supervision, C.C. and X.S.; project administration, C.C., W.W. and X.S.; funding acquisition, C.C. and X.S. All authors have read and agreed to the published version of the manuscript.

Funding: This study was supported by NOAA grant NA19NES4320002 (Cooperative Institute for Satellite Earth System Studies—CISESS) at the University of Maryland/ESSIC.

Acknowledgments: The scientific results and conclusions, as well as any views or opinions expressed herein, are those of the author(s) and do not necessarily reflect those of NOAA or the Department of Commerce.

Conflicts of Interest: The authors declare no conflict of interest.

References

1. Lee, T.; Miller, S.; Schueler, C.; Miller, S. NASA MODIS previews NPOESS VIIRS capabilities. *Weather Forecast.*, **2006**, *21*, 649–655.
2. Vargas, M.; Miura, T.; Shabanov, N.; Kato, A. An initial assessment of Suomi NPP VIIRS vegetation index EDR. *J. Geophys. Res. Atmos.*, **2013**, 118, 12301-12316.
3. Key, J.R.; Mahoney, R.; Liu, Y.; Romanov, P.; Tschudi, M.; Appel, I.; Maslanik, J.; Baldwin, D.; Wang, X.; and Meade, P. Snow and ice products from Suomi NPP VIIRS. *J. Geophys. Res. Atmos.*, **2013**, 118, 12816-12830.
4. Petrenko, B.; Ignatov, A.; Kihai, Y.; Stroup, J.; Dash, P. Evaluation and selection of SST regression algorithms for JPSS VIIRS. *J. Geophys. Res. Atmos.*, **2014**, 119, 4580-4599.
5. Cao, C.; Xiong, J.; Blonski, S.; Liu, Q.; Uprety, S.; Shao, X.; Bai, Y.; Weng, F. Suomi NPP VIIRS sensor data record verification, validation, and long-term performance monitoring. *J. Geophys. Res. Atmos.*, **2013**, 118, 11,664-11,678.
6. Cao, C.; DeLuccia, F.; Xiong, X.; Wolfe, R.; Weng, F. Early On-orbit Performance of the Visible Infrared Imaging Radiometer Suite (VIIRS) onboard the Suomi National Polar-orbiting Partnership (S-NPP) Satellite. *IEEE Trans. on Geosci. and Remote Sens.*, **2014**, 52, 1142-1156.
7. Cao, C.; Zhang, B.; Shao, X.; Wang, W.; Uprety, S.; Choi, T.; Blonski, S.; Gu, Y.; Bai, Y.; Lin, L.; Kalluri, S. Mission-Long Recalibrated Science Quality Suomi NPP VIIRS Radiometric Dataset Using Advanced algorithms for Time Series Studies. *Remote Sens.*, **2021**, 13, 1075.
8. Uprety, S.; Cao, C.; Xiong, X.; Blonski, S.; Wu, A.; Shao, X. Radiometric Inter-comparison between Suomi NPP VIIRS and Aqua MODIS Reflective Solar Bands using Simultaneous Nadir Overpass in the Low Latitudes. *J. Atmos. Oceanic Technol.*, **2013**, 30, 2720-2736.
9. Liang, X.; Ignatov, A. AVHRR, MODIS and VIIRS radiometric stability and consistency in SST bands. *J. Geophys. Res. Oceans*, **2013**, 118, 3161- 3171.
10. Madhavan, S.; Brinkmann, J.; Wenny, B.N.; Wu, A.; Xiong, X. Evaluation of VIIRS and MODIS Thermal Emissive Band calibration stability using ground target. *Remote Sens.*, **2016**, 8, 158.
11. Hulley, G.C.; Malakar, N.K.; Islam, T.; Freepartner, R. J. NASA's MODIS and VIIRS Land surface temperature and emissivity products: A long-term and consistent earth system data record. *IEEE J. Sel. Topics Appl. Earth Observat. Remote Sens.*, **2018**, 11, 522-535.
12. Skakun, S.; Justice, C.O.; Vermote, E.; Roger, J.C. Transitioning from MODIS to VIIRS: An analysis of inter-consistency of NDVI data sets for agricultural monitoring. *Int. J. Remote Sens.*, **2018**, 39, 971-992.
13. Xiong, X.; Butler, J.; Chiang, K.; Efremova, B.; Fulbright, J.; Lei, N.; Mcintire, J.; Oudrari, H.; Sun, J.; Wang, Z.; Wu, A. VIIRS on-orbit calibration methodology and performance. *J. Geophys. Res. Atmos.*, **2014**, 119, 5065-5078.
14. Efremova, B.; McIntire, J.; Moyer, D.; Wu, A.; Xiong, X. S-NPP VIIRS thermal emissive bands on-orbit calibration and performance. *J. Geophys. Res. Atmos.*, **2014**, 119, 10,859-10,875.
15. Datla, R.; Shao, X.; Cao, C.; Wu, X. Comparison of the Calibration Algorithms and SI Traceability of MODIS, VIIRS, GOES, and GOES-R ABI Sensors. *Remote Sens.*, **2016**, 8, 126.
16. Xiong, X.; Butler, J. J. Modis and VIIRS Calibration History and Future Outlook. *Remote Sens.*, **2020**, 12, 2523.
17. Wang, W.; Cao, C.; Ignatov, A.; Liang, X.; Li, Z.; Wang, L.; Zhang, B.; Blonski, S.; Li, J. Improving the Calibration of Suomi NPP VIIRS Thermal Emissive Bands During Blackbody Warm-up/Cool-Down. *IEEE Trans. on Geosci. and Remote Sens.*, **2019**, 57, 1977-1994.
18. Wang, W.; Cao, C.; Blonski, S. A new method for characterizing NOAA-20/S-NPP VIIRS Thermal Emissive Bands Response Versus Scan Using On-Orbit Pitch Maneuver Data. *Remote Sens.*, **2019**, 11, 1624.
19. Wang, W.; Cao, C.; Blonski, S. Estimating the VIIRS Thermal Emissive Band Response Versus Scan (RVS) and Calibration Offsets Using On-Orbit Pitch Maneuver Data. *IEEE Trans on Geosci. and Remote Sens.*, **2022**, 60, 5002610.
20. Shrestha, A.; Xiong, X. Tracking long-term stability of MODIS thermal emissive bands response versus scan-angle using Dome C observations. In Proceedings of SPIE 10986, Algorithms, Technologies, and Applications for Multispectral and Hyperspectral Imagery XXV, 109861W, 14 May 2019.

 doi:10.20944/preprints202402.1582.v1

21. Liu, T.; Xiong, X.; Shao, X.; Chen, Y.; Wu, A.; Chang, T.; Shrestha, A. Evaluation of aqua MODIS thermal emissive bands stability through radiative transfer modeling. *Appl. Remote Sens.*, **2021**, 15, 024502.
22. Chen, Y.; Weng, F.; Han, Y.; Liu, Q. Validation of the Community Radiative Transfer Model (CRTM) by using CloudSat data. *J. Goephys. Res.*, **2008**, 113, D00A03.
23. Chen, Y.; Han, Y.; Weng, F. Comparison of two transmittance algorithms in the Community Radiative Transfer Model: Application to AVHRR. *J. Geophys. Res.*, **2012**, 117, D06206.
24. Chen Y.; Han Y.; van Delst, P.; Weng, F. Assessment of shortwave infrared sea surface reflection and nonlocal thermodynamic equilibrium effects in the community radiative transfer model using IASI data. *J. Atmos. Oceanic Technol.*, **2013**, 30, 2152–2160.
25. Liu, Q.; Boukabara, S. Community radiative transfer model (CRTM) applications in supporting the Suomi national polar-orbiting partnership (SNPP) mission validation and verification. *Remote Sens. Environ.*, **2014**, 140, 744–754.
26. Zou, C.Z.; Goldberg, M.D.; Hao, X.-J. New generation of U.S. satellite microwave sounder achieves high radiometric stability performance for reliable climate change detection. *Science Advances*, **2018**, 4, eaau0049.